# Identification of the ADPR binding pocket in the NUDT9 homology domain of TRPM2

Peilin Yu,<sup>1,2\*</sup> Xiwen Xue,<sup>3\*</sup> Jianmin Zhang,<sup>1</sup> Xupang Hu,<sup>1</sup> Yan Wu,<sup>1</sup> Lin-Hua Jiang,<sup>4,5,6</sup> Hongwei Jin,<sup>3</sup> Jianhong Luo,<sup>1</sup> Liangren Zhang,<sup>3</sup> Zhenming Liu,<sup>3</sup> and Wei Yang<sup>1</sup>

Activation of the transient receptor potential melastatin 2 (TRPM2) channel occurs during the response to oxidative stress under physiological conditions as well as in pathological processes such as ischemia and diabetes. Accumulating evidence indicates that adenosine diphosphate ribose (ADPR) is the most important endogenous ligand of TRPM2. However, although it is known that ADPR binds to the NUDT9 homology (NUDT9-H) domain in the intracellular C-terminal region, the molecular mechanism underlying ADPR binding and activation of TRPM2 remains unknown. In this study, we generate a structural model of the NUDT9-H domain and identify the binding pocket for ADPR using induced docking and molecular dynamics simulation. We find a subset of 11 residues—H1346, T1347, T1349, L1379, G1389, S1391, E1409, D1431, R1433, L1484, and H1488—that are most likely to directly interact with ADPR. Results from mutagenesis and electrophysiology approaches support the predicted binding mechanism, indicating that ADPR binds tightly to the NUDT9-H domain, and suggest that the most significant interactions are the van der Waals forces with S1391 and L1484, polar solvation interaction with E1409, and electronic interactions (including  $\pi$ - $\pi$  interactions) with H1346, T1347, Y1349, D1431, and H1488. These findings not only clarify the roles of a range of newly identified residues involved in ADPR binding in the TRPM2 channel, but also reveal the binding pocket for ADPR in the NUDT9-H domain, which should facilitate structure-based drug design for the TRPM2 channel.

#### INTRODUCTION

The Journal of General Physiology

The transient receptor potential melastatin 2 (TRPM2) channel is a nonselective Ca<sup>2+</sup>-permeable cation channel with a broad sensitivity to many factors such as Ca<sup>2+</sup>, phosphatidylinositol bisphosphate, and temperature (Starkus et al., 2007; Tóth and Csanády, 2012; Song et al., 2016; Tan and McNaughton, 2016). Extensive evidence has demonstrated that TRPM2 functions as a sensor for oxidative stress (Jiang et al., 2010). Several recent studies using transgenic mice have revealed an important role for the TRPM2 channel in processes including insulin secretion (Uchida et al., 2011; Manna et al., 2015), generation of proinflammation cytokines (Yamamoto et al., 2008; Di et al., 2012), delayed neuronal death (Alim et al., 2013; Ye et al., 2014), ischemic kidney injury (Gao et al., 2014), protection of cardiac ischemia-reperfusion damage (Miller et al., 2014), and

The homotetrameric TRPM2 channel belongs to the TRP channel family. Each TRPM2 subunit contains a large intracellular N terminus, the typical six transmembrane domains, and a large intracellular C terminus (Fig. 1 A). Like TRPM6 and TRPM7, TRPM2 was considered to be a channel enzyme. The NUDT9 homology (NUDT9-H) domain in TRPM2 C terminus is homologous to the NUDT9 adenosine diphosphate ribose (ADPR) hydrolase (~50% similarity). TRPM2 activation by ADPR was originally proposed to be mediated by an enzymatic process in which NUDT9-H binds ADPR and converts it to AMP and ribose-5-phophate (R5P; Perraud et al., 2001, 2003). However, this view was refuted by recent work (Tóth et al., 2014; Iordanov et al., 2016), which demonstrated that TRPM2 does not possess

<sup>© 2017</sup> Yu et al. This article is distributed under the terms of an Attribution–Noncommercial–Share Alike–No Mirror Sites license for the first six months after the publication date (see http://www.rupress.org/terms/). After six months it is available under a Creative Commons License (Attribution–Noncommercial–Share Alike 4.0 International license, as described at https://creativecommons.org/licenses/by-nc-sa/4.0/).



<sup>&</sup>lt;sup>1</sup>Department of Neurobiology, Key Laboratory of Medical Neurobiology of the Ministry of Health of China, Zhejiang University School of Medicine, Hangzhou, Zhejiang 310058, China

<sup>&</sup>lt;sup>2</sup>Department of Toxicology, School of Public Health, Zhejiang University, Hangzhou, Zhejiang 310058, China

<sup>&</sup>lt;sup>3</sup>State Key Laboratory of Natural and Biomimetic Drugs, School of Pharmaceutical Sciences, Peking University, Beijing 100191, China

<sup>&</sup>lt;sup>4</sup>School of Biomedical Sciences, Faculty of Biological Sciences, University of Leeds, Leeds LS2 9JT, England, UK

<sup>&</sup>lt;sup>5</sup>Department of Physiology and Neurobiology and <sup>6</sup>Sino-UK Brain Function Laboratory, Xinxiang Medical University, Henan 453003, China

sepsis (Qian et al., 2014). Therefore, it is critical to understand the mechanism of TRPM2 channel activation during oxidative stress.

<sup>\*</sup>P. Yu and X. Xue contributed equally to this paper.
Correspondence to Wei Yang: yangwei@zju.edu.cn; or Zhenming Liu: zmliu@bjmu.
edu.cn

Abbreviations used: ADPR, adenosine diphosphate ribose;  $EC_{50}$ , half-maximal effective concentration; GBSA, generalized Born surface area; HEK, human embryonic kidney; IFD, induced-fit docking; MD, molecular dynamic; MM, molecular mechanics; NUDT9-H, NUDT9 homology; VDW, van der Waals.

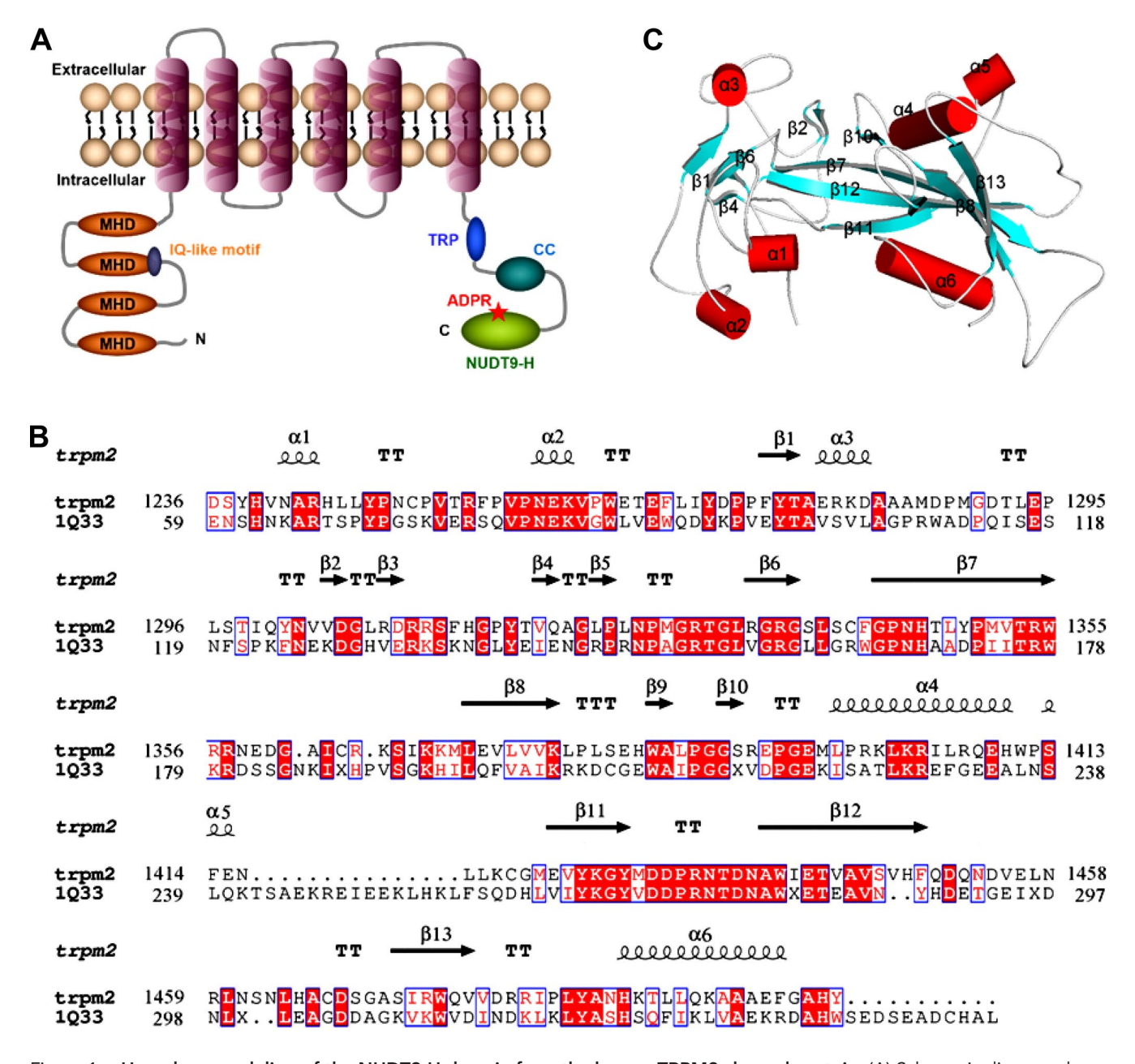


Figure 1. Homology modeling of the NUDT9-H domain from the human TRPM2 channel protein. (A) Schematic diagram showing the membrane topology of the TRPM2 channel proteins. Important domains are labeled in the figure. (B) Sequence alignments of the human NUDT9 and NUDT9-H domain. Red shading with purple border denotes identical residues, and white shading with purple border denotes similarities. (C) Ribbon presentation of the homology models of the NUDT9-H domain based on the human NUDT9 structure. The  $\alpha$ -helices,  $\beta$ -sheets, and loops are labeled in red, cyan, and gray, respectively.

ADPR hydrolase activity. Nevertheless, binding of ADPR to the NUDT9-H domain is essential for the channel opening (Perraud et al., 2001; Sano et al., 2001; Csanády and Törocsik, 2009; Tóth and Csanády, 2012). An early mutagenesis study had proposed that several residues in the NUDT9-H domain (e.g., the Nudix motif) may be engaged in ADPR binding and/or activation of the TRPM2 channel (Perraud et al., 2005), whereas the precise and whole perspective of ADPR binding remains poorly defined.

Computer-aided modeling techniques, in particular molecular dynamic (MD) simulations and homology modeling, are powerful tools that facilitate the discovery of molecular and structural insights into both ligand–receptor interactions and ligand-induced receptor activation events. These techniques have been used in elegant combinations with site-directed mutagenesis in many previous studies, including identifying the key residues for cAMP and cGMP binding and selectivity in the cyclic nucleotide-binding domain of the

HCN2 channel (Zhou and Siegelbaum, 2007), showing GABA binding sites and conformational changes during the activation of the ionotropic GABA receptors (Ashby et al., 2012). Similar approaches enabled our previous elucidation of the structural mechanisms of capsaicin binding and gating of the TRPV1 channel (Yang et al., 2015).

Our present study aimed to define molecular interactions between ADPR and the ligand-binding pocket of TRPM2. Toward this goal, we generated a structural model of the NUDT9-H domain of the TRPM2 channel based on the structure of the human NUDT9 protein (Shen et al., 2003) and used induced docking and MD simulations to identify residues in the NUDT9-H domain that coordinate ADPR via van der Waals (VDW) forces, electrostatic interactions, and hydrophobic interactions. We provided systematic functional evidence from site-directed mutagenesis and patch clamp recording experiments that corroborate their roles in coordinating ADPR. The present study not only identified new residues in the NUDT9-H domain of the TRPM2 channel that are responsible for ADPR binding but also yielded a complete picture of ADPR in the NUDT9-H domain, which holds the promise to facilitate structure-based drug design efforts targeting the TRPM2 channel.

### MATERIALS AND METHODS

#### cDNA and cell culture

The cDNA encoding the human TRPM2 (hTRPM2) channel was provided by A. M. Scharenberg (University of Washington, Seattle, WA; Perraud et al., 2001). Human embryonic kidney (HEK) 293 cells were used to transiently express wild-type (WT) and mutant channels. Cell culture, transfection, and induced TRPM2 expression were each described previously (Yang et al., 2010, 2011; Yu et al., 2014). Mutations were introduced by site-directed mutagenesis and confirmed by sequencing. All chemicals and reagents used were purchased from Sigma-Aldrich, except as otherwise indicated.

#### Electrophysiology

Whole-cell current recordings were performed using an Axopatch 200B amplifier (Molecular Devices) at RT, as described previously (Yang et al., 2010, 2011; Yu et al., 2014). For recording ADPR-induced TRPM2 currents, the extracellular solution contained 147 mM NaCl, 2 mM KCl, 1 mM MgCl<sub>2</sub>, 2 mM CaCl<sub>2</sub>, 10 mM HEPES, and 13 mM glucose, pH 7.4. The intracellular solution contained 147 mM NaCl, 0.05 mM EGTA, 1 mM MgCl<sub>2</sub>, 10 mM HEPES, and ADPR at indicated concentrations, pH 7.3. For recording calcium-induced TRPM2 currents, the extracellular solution was the same as that used in ADPR activation; the intracellular solution contained 75 mM NaCl, 1 mM MgCl<sub>2</sub>, 10 mM HEPES, and

50 mM CaCl<sub>2</sub>, pH 7.4. For recording H<sub>2</sub>O<sub>2</sub>-induced TRPM2 currents, the extracellular and intracellular solutions were the same as that used in ADPR activation, except that 30% H<sub>2</sub>O<sub>2</sub> was added to the extracellular solution with a final concentration of 30 mM. The cell membrane potential was held at 0 mV, and a voltage ramp of 500-ms duration from -100 mV to 100 mV was applied every 5 s. Glass pipettes with a resistance of 3–5 M $\Omega$  were used. Data were acquired at 10 kHz and filtered offline during data analysis. Change of the extracellular solution was performed using an RSC-160 system (Bio-Logic Science Instruments).

### Homology modeling

The amino acid sequence of the NUDT9-H domain of the human TRPM2 protein (accession no. O94759; TRPM2\_HUMAN) was derived from the UniProt database entry, and a similarity search in Protein Data Bank (PDB) database was performed by BLAST. The crystal structure of human NUDT9 (NUDT9; PDB accession no. 1Q33, chain A) was chosen as the template in building the model for the NUDT9-H domain. Using Discovery Studio 2.5 software (Accelrys Software Inc.), we produced a sequence alignment between the NUDT9 protein (residues 59-350; PDB accession no. 1Q33) and the NUDT9-H domain (UniProt accession no. O94759, residues 1236-1503). A total of 10 models were generated using the Build Homology Models module in Discovery Studio. The final model was chosen by considering probability density functions and discrete optimized protein energy values and further validated using PROCHECK and Profile-3D (Laskowski et al., 1993). Interatomic clashes were removed by 1,500 steps of steepest descent minimization, followed by 1,000 steps of conjugate gradient minimization in a solvated, neutralized simulation box with positional restraints applied to the  $C_{\alpha}$  atoms.

#### Docking

The induced-fit docking (IFD) protocol in Glide was used (Friesner et al., 2004). In IFD, the flexibility of the receptor was taken into account by combining a series of Glide and Prime processes. In the preliminary Glide docking step, the VDW radii scaling factor was set at 0.5 by default, and a maximum of 80 poses per ligand was retained. In the subsequent Prime induced-fit section, the residues within a 5-Å vicinity of the ligand were refined, whereas the others were fixed. The receptor-ligand complexes were energy minimized to an induced-fit conformation. Finally, the best receptor-ligand complex was identified using a composite scoring function with the Glide XP scoring mode adopted for docking calculations. The R1433, G1389, and H1488 residues were set as the edges of the docking pocket in an  $18 \times 18 \times 18$ –Å cube, and induced docking was subsequently performed for ADPR with the NUDT9-H domain of human TRPM2.

#### MD simulations

The structure of ADPR complexed with the NUDT9-H domain produced by the IFD procedure was explored with MD simulations. MD calculations were performed using the AMBER 11 software suite (University of California, San Francisco, San Francisco, CA). The general AMBER force field (gaff) and the ff99SB force field were used for the protein and ligand, respectively. To obtain parameters for the small molecules, ab initio quantum chemical methods were employed using Gaussian09 program (Gaussian, Inc.). The geometries were fully optimized, and the electrostatic potentials around them were determined at HF/6-31G\* level of theory. Subsequently, the atomic partial charges of the small molecules were obtained by the RESP fitting technique in AMBER 11 (University of California, San Francisco). The charges of protein ionizable groups were found to be in the standard protonation state at neutral pH. The protein-ligand complex was solvated with TIP3P water molecules in a periodically repeating truncated octahedral box. The net charge of the system was brought to neutrality and physiological ionic strength (0.15 M) by addition of dissociated NaCl, keeping an 8-Å distance away from any solute atom. The particle mesh Ewald algorithm was used to handle the long-range electrostatics in the molecular minimization and MD simulations. Before the MD simulations, each system was relaxed using a two-stage minimization strategy: the small molecules and water molecules were first subjected to 1,000 cycles of minimization with the protein backbone constrained (50 kcal  $\cdot$  mol<sup>-1</sup>  $\cdot$  Å<sup>-2</sup>), and the whole system was minimized by 2,000 cycles of steepest descent minimization without constrain. After minimization, each system was gradually heated in the canonical ensemble from 0 to 300 K over a period of 50 ps, followed by a 20-ns isobaric-isothermal MD simulation with a target temperature of 300 K and a target pressure of 1 atm. The SHAKE procedure was used to constrain all bonds involving hydrogen atoms. The time step was set to 2 fs. The PMEMD program in AMBER 11 was used for the molecular mechanics (MM) optimization and MD simulations. A 15-ns data production run was performed in the isobaric-isothermal ensemble with positional restraints imposed on the last three C-terminal  $C_{\alpha}$  atoms of each subunit (1,000  $kJ \cdot mol^{-1} \cdot nm^{-2}$ ), to mimic the presence of the transmembrane domain. Unless otherwise stated, statistics describing ligand motions and intermolecular interactions refer to the mean ± SEM value, as averaged over all 20 independent binding sites. The coordinates were saved every 10 ps during the MD sampling process.

# MM/generalized Born surface area (GBSA) binding free energy calculations

For all of the calculations below, a total of 50 snapshots from 13–15 ns were evenly extracted from the single MD trajectory at a time interval of 40 ps. The absolute

binding free energy ( $\Delta G_{binding}$ ) was then predicted by applying the MM/GBSA approaches according to the following equation (Massova and Kollman, 2000):

$$\Delta G_{binding} = \overline{G}_{complex} - (\overline{G}_{protein} + \overline{G}_{ligand}) = \Delta E_{MM} + \Delta G_{solv} - T\Delta S,$$

where  $G_{\text{complex}}$ ,  $G_{\text{protein}}$ , and  $G_{\text{ligand}}$  represent the free energies of the complex, protein, and ligand, respectively.  $\Delta E_{MM}$  is the gas-phase interaction energy calculated using the sander program in AMBER 11, including the internal, electrostatic, and VDW energies, and the internal energy was cancelled based on the single MD trajectory. The solvation free energy  $\Delta E_{solv}$  consists of both the polar and nonpolar parts, which were denoted as  $\Delta G_{GB}$  and  $\Delta G_{SA}$ , respectively.

### MM/GBSA binding energy decomposition analysis

To illustrate the interactions between each residue and ADPR, we performed MM/GBSA decomposition analysis supported by the mm\_pbsa module in AMBER 11. The binding interaction of each residue–small-molecule pair consists of four components: the VDW contribution ( $\Delta G_{vdw}$ ), the electrostatic contribution ( $\Delta G_{ele}$ ), the polar contribution of desolvation ( $\Delta G_{GB}$ ), and the nonpolar contribution of desolvation ( $\Delta G_{SA}$ ).  $\Delta G_{vdw}$  and  $\Delta G_{ele}$  were calculated using the sander program in AMBER 11. A total of 50 snapshots extracted from 13 to 15 ns MD trajectory was used for the calculations of all energy components.

## Biotinylation assay and Western blot

Biotinylation assays and Western blot were conducted as previously described (Lu et al., 2015; Zhang et al., 2015). In brief, after transfection for 24–36 h, HEK293 cells were rinsed with ice-cold PBS. The cells were subsequently incubated with a fresh preparation of 0.5 mg/ ml Sulfo-NHS-SS-Biotin (Thermo Fisher Scientific) dissolved in PBS with Tween-20 for 30 min. Subsequently, unreacted biotin was quenched with PBS containing 100 mM glycine. The cells were lysed with RIPA buffer (10 mM Tris, 150 mM NaCl, 1 mM EDTA, 0.1% SDS, 1% Triton X-100, and 1% sodium deoxycholate, pH 7.4) and subjected to centrifugation at 12,000 g for 15 min. The resulting supernatant was incubated with 40 µl of a 50% slurry of NeutrAvidin beads (Thermo Fisher Scientific) for 2 h at 4°C with continuous rotation. After several washes with RIPA buffer, the biotinylated proteins were eluted from the NeutrAvidin beads with 60 μl of 2× SDS sample buffer. The primary antibody used was rabbit anti-TRPM2 (Ab11168; Abcam), and the secondary antibody was goat anti-rabbit IgG-HRP (1:10,000; 31420; Thermo Fisher Scientific).

### Data analysis

Prism 5 software (GraphPad Software) was used for all statistical analyses. Electrophysiological recordings from

at least five cells were averaged and are presented in the text and figures, where appropriate, as means  $\pm$  SEM. To reduce the variation of TRPM2 currents from different batches in our data analysis, currents of the mutants were normalized with the mean maximal currents of the WT TRPM2 recorded on the same day, which were referred to as the relative currents. The half-maximal effective concentration (EC<sub>50</sub>) values were derived from fitting the concentration-response relationships to the Hill equation (Weiss, 1997).

# Online supplemental material

Fig. S1 uses Ramachandran plot analysis to validate the reliability of our homology modeling. Fig. S2 indicates that the predicted residues are highly conserved in the TRPM2 proteins of various species. Fig. S3 showed the merged figure of the model similar to the one previously proposed and our prediction.

#### RESULTS

# Homology modeling of the NUDT9-H domain and molecular docking of ADPR

The NUDT9-H domain of the TRPM2 channel (S1237-Y1503) is a close homologue of the human NUDT9 protein for which the apo structure was determined at 1.8 Å resolution (PDB accession no. 1Q33; Shen et al., 2003). Amino acid sequence alignment analysis showed that the NUDT9 and NUDT9-H domains have 52% similarity and 35% identity (Fig. 1 B), which is above the generally accepted threshold of 30% of sequence identity for modeling reliability (Ashby et al., 2012). The location of  $\alpha$ -helixes,  $\beta$ -sheets, and loops in both proteins are well conserved (Fig. 1 C). The reliability of our homology modeling was validated by Ramachandran plot analysis (Fig. S1). Further refinement of the structural model by energy minimization resulted in 99.6% of the residues falling within the favored/allowed region of the Ramachandran plot. The tertiary structural model of the NUDT9-H domain is very similar to that of NUDT9 (Fig. 2 A).

To investigate the configuration of the bound ADPR and its interaction with the ligand-binding domain, ADPR (for which the chemical structure is shown in Fig. 2 B) was docked into the structural model. The results predicted that ADPR takes a saddle-like conformation inside the NUDT9-H domain. A subset of 11 residues were identified to interact with ADPR. Specifically, the terminal ribose ring in ADPR makes direct contacts with L1379, G1389, and E1409; the pyrophosphate group interacts with H1346, T1347, S1391, and R1433; and the adenosine base interacts T1349, D1431, L1484, and H1488 (Fig. 2, B and C). Five of these residues—T1349, L1379, S1391, R1433, and H1488—have been previously proposed to participate in ADPR binding, which was based on the observed

interactions between the corresponding residues in the NUDT9 protein and R5P in the crystal complex (Shen et al., 2003).

# Validating the stability of modeled ADPR/NUDT9-H complex with MD simulations

MD simulations were performed for the ADPR-bound state of the NUDT9-H domain. We performed 15-ns simulations of the ADPR/NUDT9-H complex. The root mean square deviations of protein backbone atoms for the complex reached equilibrium after 9 ns at ~5 Å (Fig. 2 D). The bound ligands remained in their original conformation during the 15-ns MD simulations. No large alterations in the secondary structures were detected during the simulations, further demonstrating the stability of this ligand-binding pocket. Furthermore, our simulations provide insight into the local, shortrange interactions that occur between ADPR and particular residues in the NUDT9-H domain. Based on the frames from the 15-ns MD simulation trajectory, the component energies of ADPR binding to the NUDT9-H domain were calculated, including the ELE (electrostatic energy), VDW (VDW energy), INT (bond, angle, and dihedral energies), mean electrostatic (Coulombic) and VDW potential energies of interaction GBSUR (hydrophobic contribution to solvent free energy for generalized Born calculations), as well as the GB (reaction field energy calculated by GB; Table 1). Moreover, the interactions between ADPR and each of the 11 residues identified in the molecular docking were assigned into VDW force, electrostatic interaction, polar solvation, and nonpolar solvation groupings, and their contributions to the binding energy for ADPR were calculated (Table 2). This analysis provided an index of the relative contributions of different residues to the strength of ligand binding. MM/GBSA binding free energy calculations supported that the 11 residues make strong interactions with ADPR, which were subject to further mutagenesis study.

# Alanine scanning validated our predicted binding clefts for ADPR

To obtain experimental evidence to verify the predicted binding pockets of ADPR, we initially performed alanine scanning of the 11 critical residues identified by the molecular docking and MD simulations. Whole-cell recordings were performed to measure ADPR-induced currents in HEK293 cells expressing hTRPM2 WT or mutant channels. A representative current recording of the WT channel activated by ADPR is shown in the left panel of Fig. 3 A, with the voltage-dependent current measured with the ramp protocol shown in the right panel. The I-V relationship exhibits linearity and strong sensitivity to inhibition by acidic pH, as reported previously (Yang et al., 2010). Previous studies using whole-cell recording have determined the EC50 value of ADPR

Table 1. Binding energy of ADPR with NUDT9-H

Energy	Mean	SD	
	kcal/mol	kcal/mol	
ELE (electrostatic energy)	-44.42	7.33	
VDW (VDW energy)	-45.09	4.10	
INT (bond, angle, dihedral energies)	0.00	0.00	
GAS (ELE + VDW + INT)	-89.51	7.13	
GBSUR (hydrophobic contributor to solvent free energy for GB calculations)	-6.04	0.37	
GB (reaction field energy calculated by GB)	71.03	4.94	
GBSOL (GBSUR + GB)	65.00	4.81	
GBELE (GB + ELE)	26.61	4.67	
GBTOT (GBSOL + GAS)	-24.52	3.51	

from the concentration-response relationship to be 10 to 90  $\mu$ M (Perraud et al., 2001; Starkus et al., 2007). Our measurements yielded an estimate of the EC<sub>50</sub> value of 40  $\mu$ M; the consistency with previous studies further val-

idated our system. Two concentrations, at approximately  $EC_{10}$  (3 µM) and  $EC_{90}$  (100 µM) of ADPR, were used to activate the mutant forms of TRPM2. None of the mutants, with the exception of S1391A and L1379A, were completely activated by ADPR (Fig. 3 C), supporting the idea that these residues are critical for ADPR binding. To examine whether the observed loss of function in mutants was because of defective membrane trafficking, a biotinylation assay was used to determine surface expression of the mutant proteins. All of the nonfunctional mutants were delivered to the cell surface, as with the WT hTRPM2 channel (Fig. 3 D).

Given that most of these 11 residues have not been investigated previously, we next addressed their roles in ADPR-induced activation of the hTRPM2 channel by characterizing the effects of point mutations on channel function. To avoid current variation resulting from variable expression level of WT or mutants in different batches of cells, we controlled the experimental condition as follows: (a) strictly 50 ng EGFP and 1 µg WT or

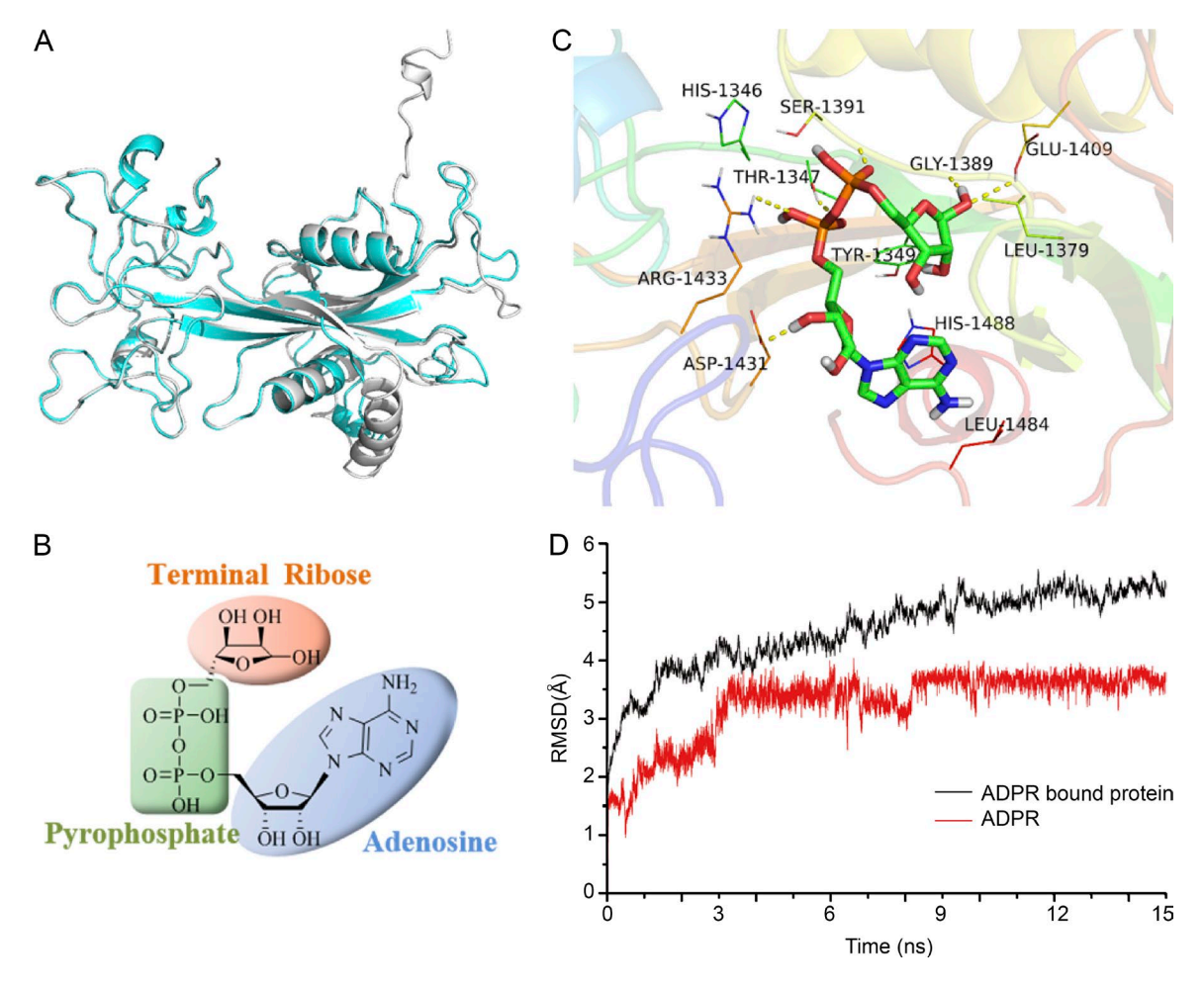


Figure 2. **Docking of ADPR to the NUDT9-H domain of TRPM2.** (A) The tertiary structure of human NUDT9 (gray) and the model of NUDT9-H domain. (B) Chemical structures of ADPR. The terminal ribose is circled with orange; the pyrophosphate is boxed with green; and the adenosine is circled with blue. (C) Ribbon presentation of the binding pocket in the NUDT9-H domain (gray) docked with ADPR. The key residues mediating binding of ADPR are highlighted. (D) MD simulation of the NUDT9-H domain in complex with ADPR: the root mean square deviation (RMSD) of ADPR (red) and ADPR-binding protein (black), respectively.

Residues	VDW	Electrostatic	Polar solvation	Nonpolar solvation	Total
	kcal/mol	kcal/mol	kcal/mol	kcal/mol	kcal/mol
HIS1346	-1.40	-1.60	2.10	-0.23	-1.13
ΓHR1347	-0.55	-6.53	0.23	-0.06	-6.91
ΓYR1349	-1.85	-2.99	2.94	-0.11	-2.01
LEU1379	-1.04	0.11	-0.49	-0.17	-1.60
GLY1389	-0.99	-3.22	1.01	-0.20	-3.40
SER1391	-0.14	0.27	-0.03	-7.32E-05	0.10
GLU1409	-0.09	1.08	-0.73	-0.01	0.26
ASP1431	-0.67	-3.14	3.98	-0.13	0.04
ARG1433	-1.17	0.30	0.72	-0.30	-0.45
LEU1484	-0.04	-0.10	-0.05	0.00	-0.18
HIS1488	-2.07	-1.16	0.93	-0.20	-2.51

Table 2. Binding energy values of residues interacting with ADPR in the NUDT9-H domain

mutant hTRPM2 plasmids were mixed and used for transfecting HEK293 cells; (b) electrophysiology experiments were performed 24–36 h after transfection; and (c) cells with similar green fluorescence intensity and cell size were chosen for patch-clamp recording. In addition, considering that some of the mutants failed to yield a saturated response even at millimolar concentrations of ADPR, all currents from the mutant channels were normalized to the maximal currents of WT hTRPM2 recorded on the same day and referred to as the relative currents.

# Residues interacting with the terminal ribose of ADPR

ADPR is composed of three moieties: a terminal ribose, a pyrophosphate, and an adenosine (Fig. 2 B). Our results so far predicted that each of these moieties interacts with a different subset of residues in the NUDT9-H domain. Therefore, each of the residues was individually mutated to selected amino acids depending on the nature of the predicted interactions they form with ADPR. The mutational effects on ADPR-induced TRPM2 channel activation were evaluated.

L1379, G1389, and E1409 were predicted to interact with the terminal ribose of ADPR (Fig. 4 A). Sequence alignments indicate that these residues are highly conserved in the TRPM2 proteins of various species (Fig. S2). E1409 was predicted in our MD simulation to have a strong polar solvation interaction between its hydroxyl oxygen atom and the terminal ribose of ADPR (Table 2). In support of this prediction, the E1409A mutation caused a dramatic increase in the EC<sub>50</sub> value for ADPR (Fig. 4 B and Table 3). Furthermore, we produced the E1409Q mutant that would disrupt electrostatic interaction but maintain polar hydrogen bonding with the ligand. In contrast to E1409A, the E1409Q mutation caused a strong increase in sensitivity to ADPR (Fig. 4 B and Table 3), supporting the importance of the polar solvation interaction between this residue and the terminal ribose of ADPR.

L1379 was predicted to interact with the terminal ribose via VDW forces (Table 2). The L1379A mutation,

which shortened the side chain of leucine, had no significant effect on the sensitivity to ADPR (Table 3), suggesting that VDW force might not be critical for L1379. However, introducing a polar group by a L1379S mutation not only increased the sensitivity to ADPR, but also resulted in a much shallower slope of the concentration-response curve (Fig. 4 C and Table 3). These strong effects, although not necessarily supporting the existence of specific VDW interactions, suggest the prediction that L1379 directly participates in mediating ligand–host interaction.

Our simulation suggested the occurrence of an electrostatic interaction between the carboxyl group of G1389 and the hydroxyl group of the terminal ribose ring of ADPR. To examine this prediction, G1389 was mutated to alanine to add a methyl group to glycine, which has the smallest side chain among all amino acids. Our result showed that the G1389A mutant failed to be activated by ADPR (Fig. 3 C). This result, although consistent with our prediction that G1389 is critical for ADPR binding, prevented us from constructing the concentration-response relationship as we did for mutants of E1409 and L1379. To further exclude the possibility that G1389A mutation affected the channel gating function, we tested with whole-cell patch recording whether this mutant could be activated by calcium or H<sub>2</sub>O<sub>2</sub>, which were previously reported to independently activate TRPM2. Consistent with our biotinylation data, G1389A mutant was found to be readily activated by calcium, confirming that this mutant retained channel function (Fig. 4, D and E). Interestingly, our data further showed that H<sub>2</sub>O<sub>2</sub> failed to induce a current from G1389A mutant (Fig. 3, F and G), which suggests that H<sub>2</sub>O<sub>2</sub> may regulate TRPM2 channel through the NUDT9-H domain. In summary, the collective results indicate that the terminal ribose of ADPR likely makes direct contacts with L1379, G1389, and E1409 in the NUDT9-H domain of TRPM2. Differences in the properties of these individual residues lead to their diverse contributions to ligand binding.

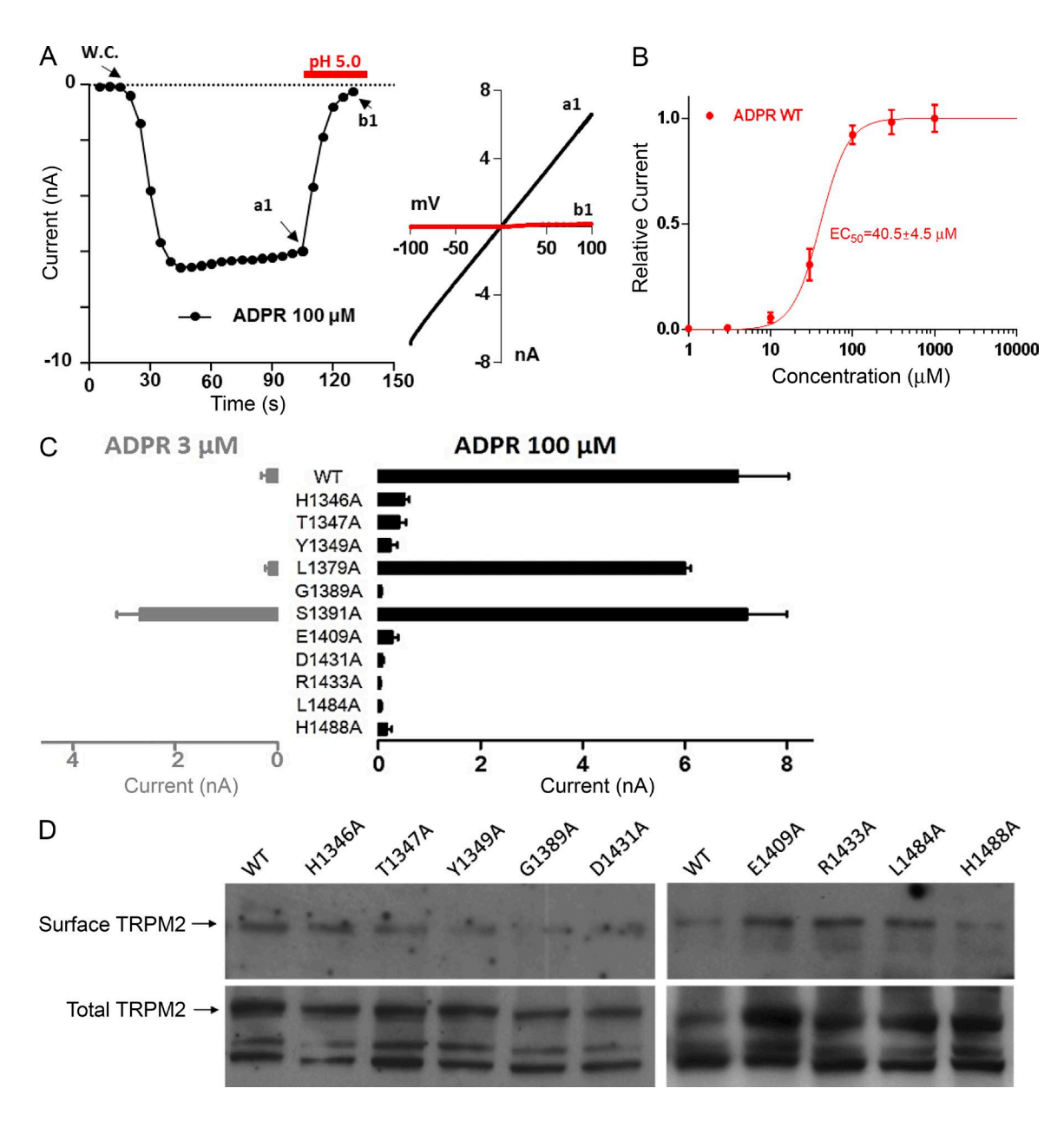


Figure 3. Alanine substitution scanning of 11 identified residues in ADPR-binding pockets. (A) 100  $\mu$ M ADPR-induced TRPM2 currents traces at -80 mV (left panel) and the I-V relationship curves (right panel, at time points indicated by a1 pointed to before pH 5.0 treatment and b1 pointed to after pH 5.0 inhibiting TRPM2 channel). W.C., whole cell. (B) The concentration–current response relationship for ADPR and the WT TRPM2 channel. Data are expressed as mean  $\pm$  SEM from seven independent repetitions. (C) Summary of the currents induced by EC<sub>10</sub> (gray) and EC<sub>90</sub> (black) concentrations of ADPR. Data are expressed as mean  $\pm$  SEM from at least five independent repetitions. (D) Biotinylation assay for surface expression of the TRPM2 and its mutants. The eight mutants that exhibited no channel function were expressed on the cell surface in HEK293 cells. The top panel shows surface expression, and the bottom panel shows total expression. Arrows indicate the specific band size of WT and the indicated TRPM2 mutants.

Residues interacting with the pyrophosphate of ADPR A previous study showed that the pyrophosphate group of ADPR is critical for ADPR binding to the NUDT9-H domain (Moreau et al., 2013). However, channel residues in the ligand-binding domain that interact with the pyrophosphate have not been identified. Our simulations identified H1346, T1347, S1391, and R1433 as the candidate residues that interact with the pyrophosphate group (Fig. 5 A). Of note, these residues are also

widely conserved (Fig. S2). Among these four residues, MD simulations suggested the imidazole ring of H1346 makes electrostatic interactions with the pyrophosphate group (Table 2). Functional tests showed that structural perturbations by either H1346A or H1346F mutation left the mutant channels completely insensitive to ADPR (Fig. 5 B), consistent with the idea that the electrostatic interactions mediated by H1346 might be critical for ADPR binding. In further support of this view, the

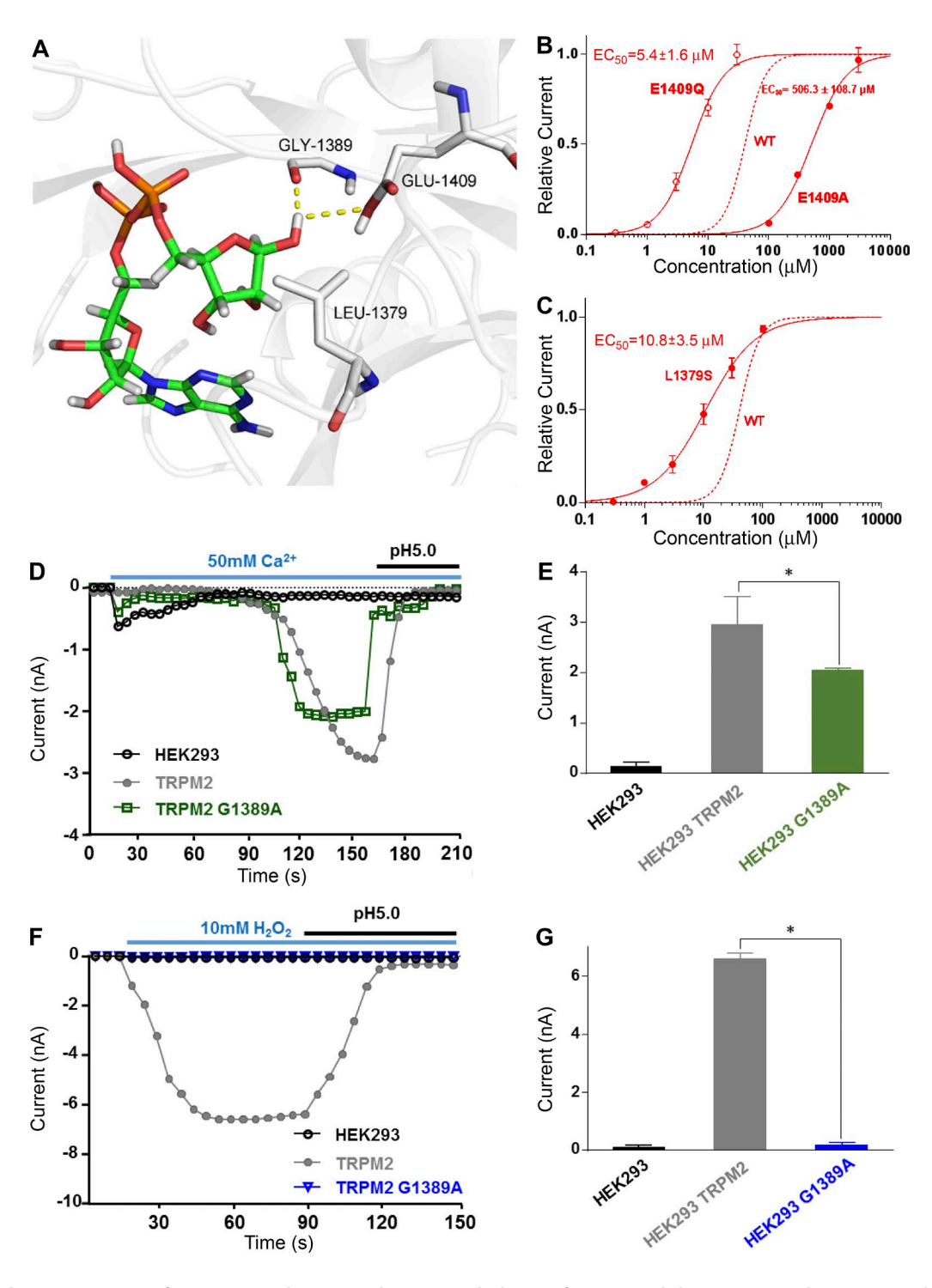


Figure 4. Characterization of interactions between the terminal ribose of ADPR and the NUDT9-H domain. (A) Ribbon presentation of the terminal ribose binding pockets in the NUDT9-H domain (gray). The interactions are denoted with yellow dashed lines. (B and C) Characterization of the ADPR concentration–current response relationship for the WT (dashed line) and indicated mutants (continuous line) of the TRPM2 channels. Data are expressed as mean  $\pm$  SEM from five independent repetitions. (D) The representative traces induced by 50 mM calcium in HEK293 blank cell, TRPM2, and G1389A mutant–transfected cells. (E) Summary of the currents in D. (F) The representative trace induced by 10 mM  $H_2O_2$  in HEK293 blank cell, TRPM2, and G1389A mutant–transfected cells. (G) Summary of the currents in F). Data in E and G are expressed as mean  $\pm$  SEM from at least six independent repetitions.

Table 3. The  $EC_{50}$  values of ADPR for the mutants in the NUDT9-H domain of TRPM2

$\mu M$ $40.5 \pm 4.5$ NF NA $V$ $112.5 \pm 6.4$ NF NA $92.9 \pm 11.2$ $115.1 \pm 13.4$ NF NA $>10 \text{ mM N}$ ND NA $10.8 \pm 3.5$ $3.5 \pm 0.2 \pm 3$	$EC_{50} \pm SEM$ Hill slope		
NF NA NF NA NF NA 112.5 ± 6.4 NF NA 92.9 ± 11.2 115.1 ± 13.4 NF NA >10 mM N ND NA 10.8 ± 3.5 3.5 ± 0.2 \$\frac{9}{2}\$			
$\begin{array}{c} V & 112.5 \pm 6.4 \\ NF \ NA \\ 92.9 \pm 11.2 \\ 115.1 \pm 13.4 \\ NF \ NA \\ > 10 \ mM \ N \\ ND \ NA \\ 10.8 \pm 3.5 \\ 3.5 \pm 0.2 \ 2 \\ \end{array}$	2.6		
NF NA 92.9 ± 11.2 115.1 ± 13.4 NF NA >10 mM N ND NA 10.8 ± 3.5 3.5 ± 0.2 \$2			
92.9 ± 11.2 115.1 ± 13.4 NF NA >10 mM N ND NA 10.8 ± 3.5 3.5 ± 0.2 2	2.0		
115.1 ± 13.4 NF NA >10 mM N ND NA 10.8 ± 3.5 3.5 ± 0.2 2			
NF NA >10 mM N ND NA 10.8 ± 3.5 3.5 ± 0.2 2	1.2		
>10 mM N ND NA 10.8 ± 3.5 3.5 ± 0.2 2	4 1.3		
ND NA 10.8 ± 3.5 3.5 ± 0.2 §			
$10.8 \pm 3.5  3.5 \pm 0.2 $	NΑ		
$3.5 \pm 0.2\%$			
	1.0		
	2.7		
$506.3 \pm 108.$	7 1.5		
$5.4 \pm 1.6$ 1	1.6		
NF NA			
>100 mM	NA		
NF NA			
NF NA			
>10 mM N	NA		
ND NA			
NF NA			
>10 mM N	NA		

NA, not applicable; ND,  $EC_{50}$  value is not significantly different from the WT, based on the measurements of currents induced by  $EC_{10}$  and  $EC_{90}$  concentrations of ADPR; NF,  $EC_{50}$  value is not defined because the mutation fails to yield a saturated response even at millimolar concentrations of ADPR.

H1346W mutation reduced the sensitivity to ADPR (Fig. 5 B), highlighting the importance of electrostatic interaction with ADPR binding as the replacement with a benzene ring by the mutation is expected to obviate the electronic property of histidine.

Our simulations predicted that T1347, located in close vicinity to H1346, is also important in the electrostatic interaction with ADPR (Table 2). To validate this prediction, we generated T1347A, T1347I, T1347F, and T1347Y mutants. T1347I mutant channels completely lost sensitivity to ADPR, whereas T1347A mutant channels yielded only a minor response to ADPR (Fig. 5 C), consistent with the expectation that eliminating the potential electrostatic interaction would substantially affect ligand-channel interaction. Moreover, the T1347F and T1347Y mutants slightly reduced sensitivity to ADPR (Fig. 5 C), which could be interpreted that the addition of a benzene ring at this position introduced steric hindrance that may interfere with the electrostatic interaction between the hydroxyl group of T1347 and ADPR. It is noted that the slopes of the ADPR concentration-response curves for both the T1347F and T1347Y mutants were substantially altered, indicating a likely change of the binding pattern (Fig. 5 C). These results together supported the notion of a critical role of the side chain of threonine in ADPR binding to the NUDT9-H domain.

VDW force interactions were predicted to occur between S1391 and the pyrophosphate group of ADPR (Table 2). Interestingly, the S1391A mutant that in-

creased the distance between the residue and ADPR had a dramatically decreased EC<sub>50</sub> for ADPR (Fig. 5 D and Table 3). Furthermore, neither the S1391F mutation, which replaced the polar hydroxyl group with a nonpolar benzene ring, nor the S1391Y mutation, which increased the length of the side chain in serine, had noticeably altered the channel sensitivity to ADPR (Fig. 5 D), suggesting that the hydroxyl group of this residue was not critical for ADPR binding. These observations are consistent with the prediction that VDW force might have a major contribution to ADPR binding at this site.

Additionally, the VDW force and a minor nonpolar solvation interaction between R1433 and the pyrophosphate of ADPR were predicted in our simulations (Table 2). This prediction appeared rather strange in that the charged residue arginine unexpectedly provides no contribution to electrostatic or polar solvation interactions. To further investigate this prediction, we produced a series of mutations to change the length, polarity, and charge characteristics of the side chain at this position. Among R1433A, R1433K, R1433L, R1433Q, and R1433G mutants, only the R1433G mutant exhibited a low affinity for ADPR, whereas all of the others had no response to ADPR (Fig. 5 E and Table 3). Although these results did not validate the accuracy of the prediction in our simulations, they are consistent with the importance of this residue for ADPR binding to the NUDT9-H domain.

Residues interacting with the adenosine region of ADPR Our simulations predicted that Y1349, D1431, L1484, and H1488 contribute in the interaction with the adenosine group of ADPR (Fig. 6 A). For Y1349, it interacts with the adenine of ADPR through a  $\pi$ - $\pi$  interaction, which is a form of electrostatic interaction. In addition, an interaction between its hydroxyl group and the terminal ribose was predicted (Fig. 6 A and Table 2). Our mutagenesis experiments showed that the Y1349F mutation did not significantly alter channel activation by ADPR (Fig. 6 B), indicating that the hydroxyl group of Y1349 contributed little to ADPR binding. However, neither Y1349A nor Y1349S mutant could be activated by ADPR (Fig. 6 B). Even the Y1349I mutant, which has the longest side chain, exhibited a very low response to ADPR. These observations suggest that the benzene ring of Y1349 is critical for ADPR binding. Our data are consistent with the idea that a  $\pi$ - $\pi$  interaction mediated by the benzene ring of Y1349 is required for ADPR binding (Fig. 6 B).

Our simulations also predicted a strong electrostatic interaction between D1431 and ADPR (Table 2). Results from mutagenesis experiments supported this prediction, as the D1431A mutation exhibited almost no response to ADPR, whereas the D1431N mutant, which neutralized the negative charge of aspartic acid,

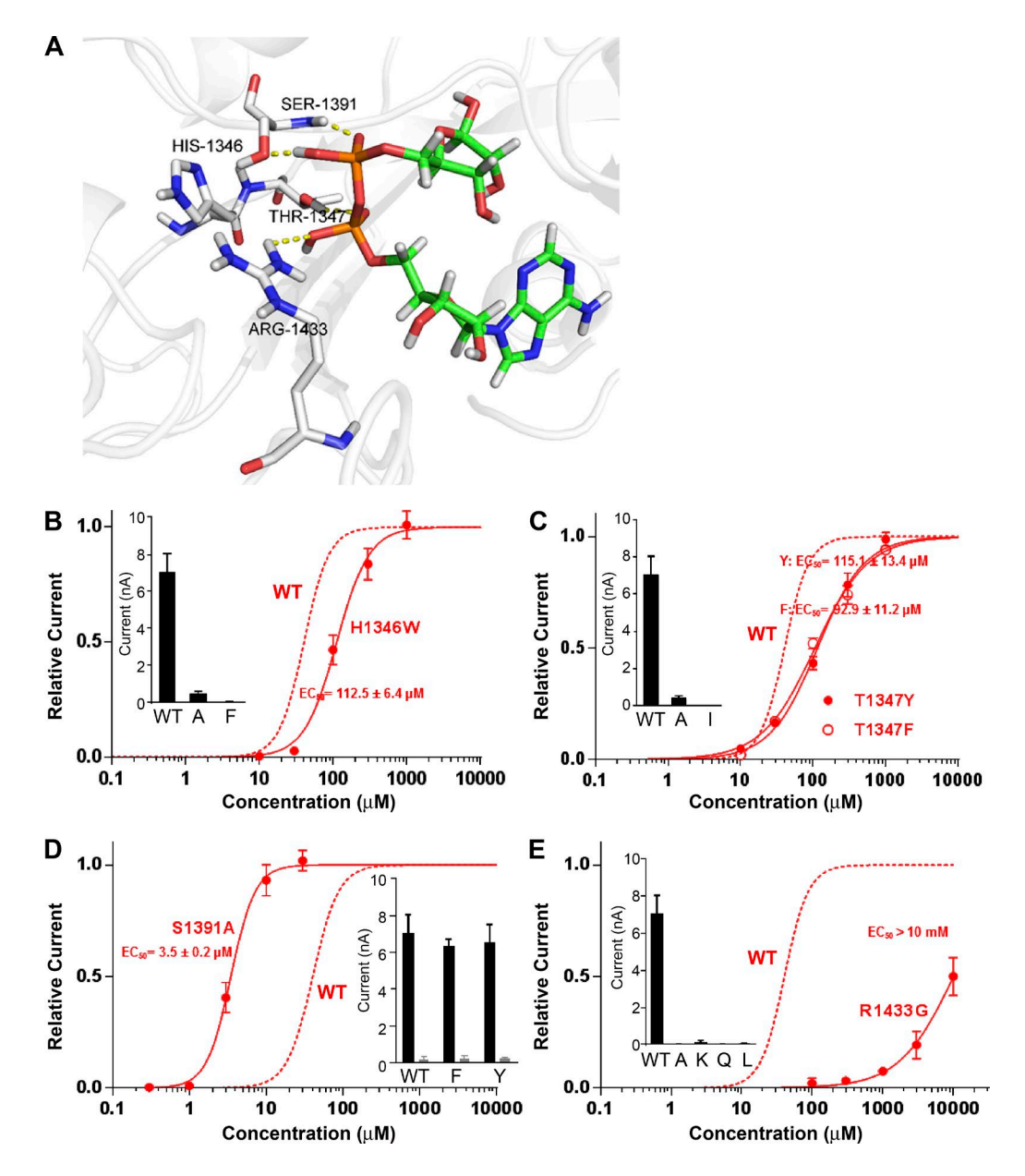


Figure 5. Characterization of interactions between the pyrophosphate of ADPR and the NUDT9-H domain. (A) Ribbon presentation of the pyrophosphate binding pockets in the NUDT9-H domain (gray). The interactions are denoted with yellow dashed lines. (B–E) Characterization of the ADPR concentration–current response relationship for the WT (dashed line) and the indicated mutant (continuous line) of the TRPM2 channels. The insets in B–E represent summary of the currents from additional mutants of the indicated residues when activated by 100  $\mu$ M (black) or 3  $\mu$ M (gray) ADPR. Data in B–E are expressed as mean  $\pm$  SEM from at least five independent repetitions.

had a much higher  $EC_{50}$  value for ADPR than that of the WT channel (Fig. 6 C and Table 3). These results support the notion that the likely electrostatic interaction from D1431 is necessary for ADPR binding to the NUDT9-H domain.

In addition, our MD simulations suggested a weak VDW force between the isobutyl side chain of L1484 and the adenosine (Table 2). The lack of channel function in the L1484A mutant, which has a decreased distance between the side chain of this residue and ADPR, supports the notion of an important role in

ADPR binding for the VDW force interaction (Fig. 3 C). In further support of this notion, when L1484 was mutated to valine that has a similar isopropyl side chain, the binding affinity of ADPR did not change (Table 3).

H1488 was predicted to interact with the adenosine of ADPR by both VDW force and electrostatic interactions (Table 2). Our mutagenesis experiments showed that the H1488F mutant that lost the positive charge on the imidazole ring of histidine had a much-reduced sensitivity to ADPR (Fig. 6 D), consistent with that dis-

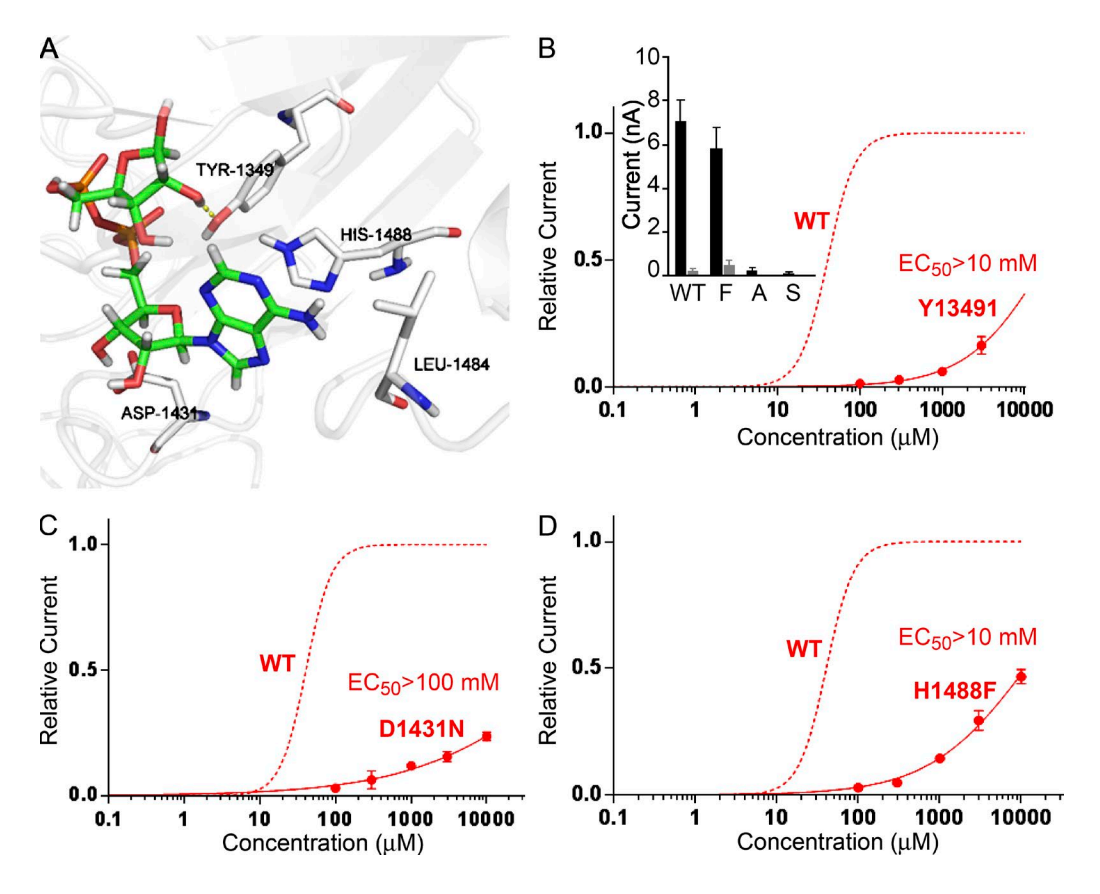


Figure 6. Characterization of interactions between the adenosine of ADPR and the NUDT9-H domain. (A) Ribbon presentation of the adenosine binding pockets in the NUDT9-H domain (gray). The interactions are denoted with yellow dashed lines. (B–D) Characterization of the ADPR concentration–current response relationship for the WT (dashed line) and the indicated mutant (continuous line) of the TRPM2 channels. The inset in B represents a summary of the currents from additional mutants of the indicated residue when activated by  $100 \mu M$  (black) or  $3 \mu M$  (gray) ADPR. Data in B–D are expressed as mean  $\pm$  SEM from five independent repetitions.

ruption of electrostatic interaction did affect the binding affinity between H1488 and ADPR.

# A working model of ADPR binding inside the NUDT9-H domain

Collectively, our mutagenesis and functional assay results not only demonstrated that most of the residues predicted in our MD simulations are indeed critical for ADPR binding, but also lent support to the idea of an interaction force between ADPR and H1346, T1347, Y1349, S1391, E1409, D1431, L1484, and H1488. A working model for ADPR binding to the NUDT9-H domain of TRPM2 that incorporates our observations is presented in Fig. 7. The identified key residues (shown in Fig. 7 C in green) define a clear outline of the binding pocket for ADPR. In this model, the molecular surface of the binding pocket contains two large cavities: one accommodates the adenine by the space parallel to the purine ring of ADPR, which is mainly formed by L1484 and H1488; the other one is formed by L1379, G1389, and E1409 to enwrap the terminal ribose of ADPR. Between these two moieties, the other critical residues of the NUDT9-H domain formed a shallower trench, with the pyrophosphate and the ribose of the adenosine of ADPR lying in it.

## DISCUSSION

In this study, we investigated binding of ADPR to the NUDT9-H domain and proposed a detailed structural model for atomic interactions that mediate ligandhost interactions. This model is not only supported by our systematic functional tests but also by results from previous studies. Indeed, recent studies have identified several residues clustered in regions of the NUDT9-H domain that are critical for ADPR-induced activation of the TRPM2 channel (Perraud et al., 2005; Du et al., 2009; Tóth et al., 2014). Although these individual sites alone could not reveal the precise and complete binding mode of ADPR within the NUDT9-H domain, when mapped on our model, it becomes clear how they may contribute to ligand binding. Based on the crystal structure of human NUDT9 and the Escherichia coli ADPRase-ADPR complex, Shen et al. (2003) initially proposed a hypothetical model of ADPR binding to the NUDT9-H domain. A subsequent

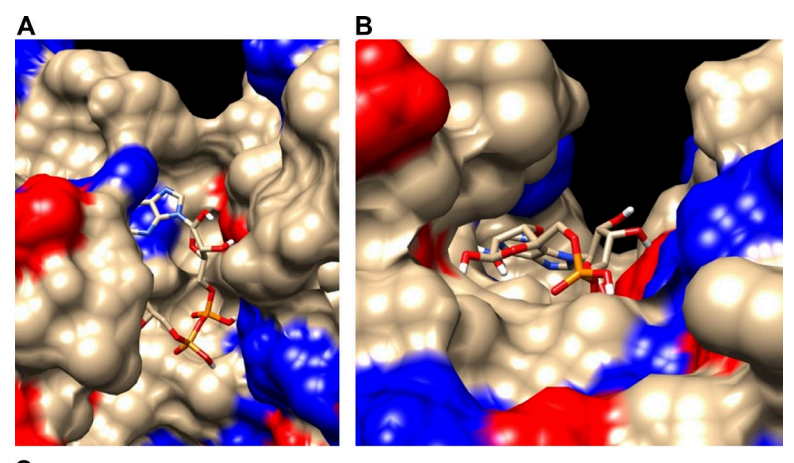
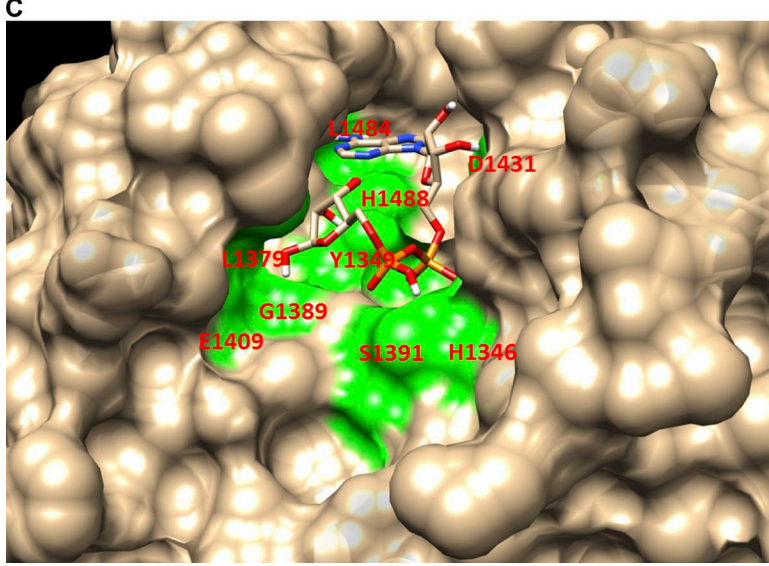


Figure 7. Binding pocket of ADPR in the NUDT9-H domain presented from different orientations. A and B show the side (A) and top view (B) of the ADPR-binding model in the NUDT9-H domain. The positively and negatively charged residues are colored in blue and red, respectively. (C) The whole view of the binding pocket of ADPR in the NUDT9-H domain. Critical residues for binding are labeled in green.



study generated a homology model of the NUDT9-H domain and docked ADPR into the anticipated AD-PR-binding pocket (Perraud et al., 2005). The docked ADPR took a different conformation in that the horseshoe-shaped molecule points its ends in the opposite direction from that of our model. In the present study, we generated a structure model of the NUDT9-H domain guided by the crystal structure of NUDT9 and defined the ligand-binding pocket formed by the NUDT9-H domain using structural modeling, ligand docking simulations, and MD simulations. Our MD simulation results predicted that 11 residues in the binding pocket interact strongly with ADPR through VDW forces, electrostatic interactions, polar solvation interactions, and nonpolar solvation interactions. By combining MD simulations with site-directed mutagenesis studies, we demonstrated that all of the identified residues in the NUDT9-H domain interact with ADPR, supporting our predicted binding pocket model for TRPM2.

The homology model of the NUDT9-H domain in our study is very similar to the model reported in a previous study (Perraud et al., 2005), which is not sur-

prising given the high sequence similarity between NUDT9-H and human NUDT9. However, our predicted ADPR binding pocket and the binding orientation of ADPR are clearly different from those in the earlier model. To test whether ADPR can bind in the previously proposed orientation, we also docked ADPR into the NUDT9-H domain in a similar orientation (Fig. 8 A). We found that this orientation yielded a much reduced docking IFD score (Table 4). To more easily compare this model with our predicted one, we merged them together (Fig. S3) and found ADPR in this orientation would interact with NUDT9-H at several additional and potentially important residues, including D1287, S1338, S1340, N1345, S1382, and I1440. Among these residues, D1287, S1340, and N1345 were previously proposed to interact with ADPR but not examined further using functional assays (Shen et al., 2003). Therefore, we mutated these residues to alanine individually and examined by patchclamp recording of ADPR-induced currents in cells expressing the mutant channels. Both the D1287A and S1340A mutant channels had normal activity induced by ADPR (Fig. 8, B–F), supporting the conclusion that

Table 4. Comparing of the IFD scoring of the model similar to the one previously proposed and our prediction

Models	Docking score	Glide gscore	Glide emodel	Prime energy	IFD score
	kcal/mol	kcal/mol	kcal/mol	kcal/mol	kcal/mol
Our prediction	-8.4	-8.4	-98.13	-3,710.1	-3,823.0
The model similar to the one previously	-5.9	-5.9	-90.7	-3,644.7	-3,750.5
proposed					

these residues have no major role in ADPR binding. Both the model proposed by Perraud et al. (2005) and our model are based on the crystallographic information of human NUDT9, which contained a ligand molecule, R5P (Shen et al., 2003). In the previous model, ADPR assumes a horseshoe-like conformation that bends over the superficial surface of the ADPR-binding pocket (Perraud et al., 2005). However, this does not match the position of R5P in the crystal structure of NUDT9. To illustrate the difference in these binding models, we highlight the critical residues (W110, N168, M216, R273, M280, and D305) identified in the Perraud model in red in our structure model (Fig. 9, A and B). In our model, ADPR locates in a deeper cleft, a position consistent with that of R5P in the cleft of the NUDT9 structure (Fig. 9, C and D). Of note, key residues that have been previously reported to interact with R5P in the crystal structure of the NUDT9 protein

are also identified in our model for ligand binding, including Y1349 (D172), L1379 (R204), E1409 (E234), R1433 (R273), and H1488 (H324) (Fig. 9, E and F). Our mutagenesis and functional results demonstrate that these residues are indeed critical sites for ADPR binding to the NUDT9-H domain. These results lend further support for the accuracy of our ADPR binding model.

To further verify our model, we also examined how compatible our ADPR-binding pocket is with the results from previously published studies. First, a recent study reported that when the 2'-hydroxyl group of ADPR was replaced with a phosphate group, it could still function as a ligand of TRPM2 (Toth et al., 2015). This can be explained by our model: there is an open space at the vicinity of the 2'-hydroxyl of ADPR that can conceivably accommodate both the extra mass and the more polar phosphate group (Fig. 7 A). Second,

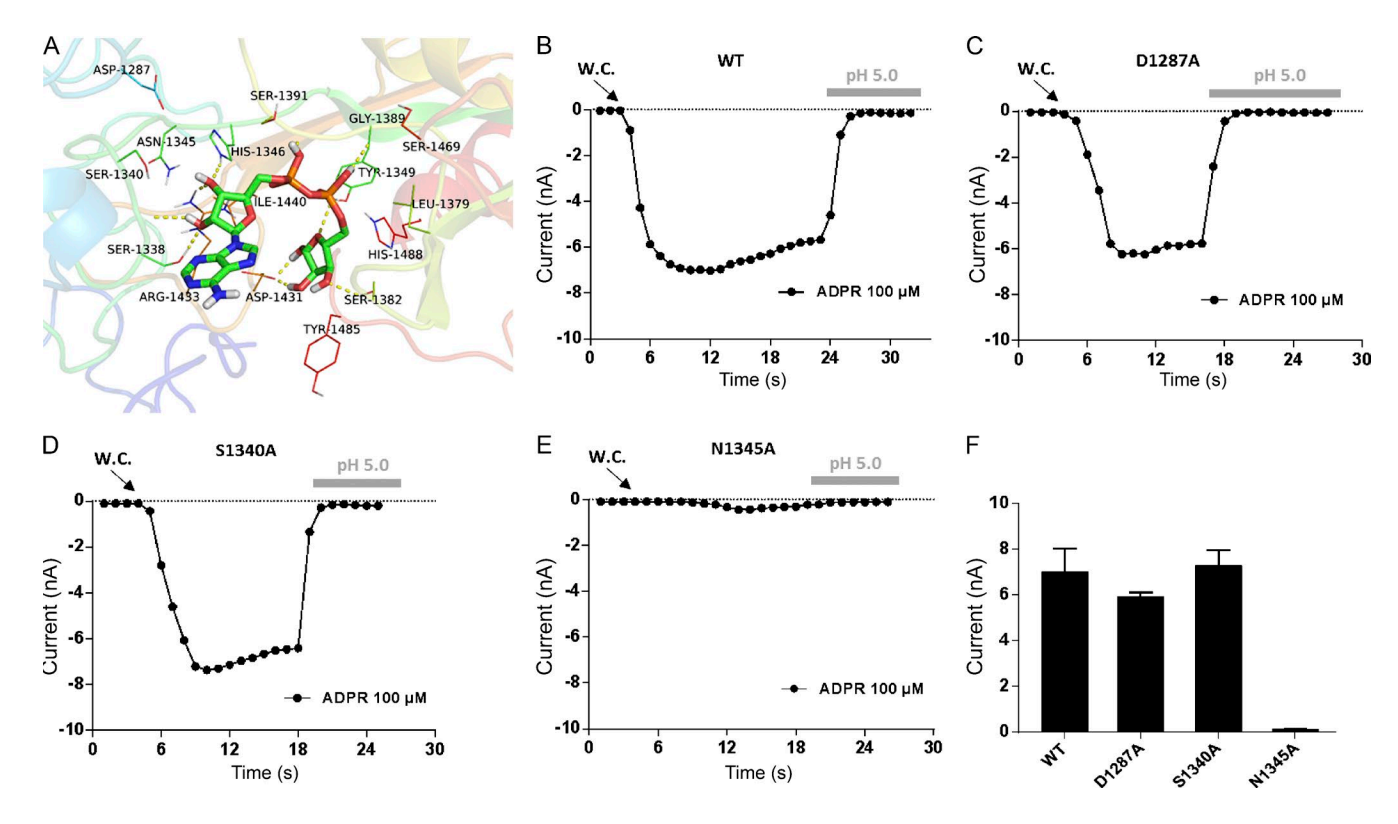


Figure 8. Evaluation of a previous model for ADPR binding to the NUDT9-H domain. (A) The previously proposed orientation of ADPR shown in the NUDT9-H domain using our present model. In this orientation, ADPR is in close proximity to several residues for which mutations did not affect binding. Current traces of WT TRPM2 (B) and mutants at three positions (C–E) predicted to interact with ADPR in the orientation shown in A. (F) Summary of the currents from the mutants at the three positions when activated by ADPR 100  $\mu$ M. Data are expressed as mean  $\pm$  SEM from at least five independent repetitions.

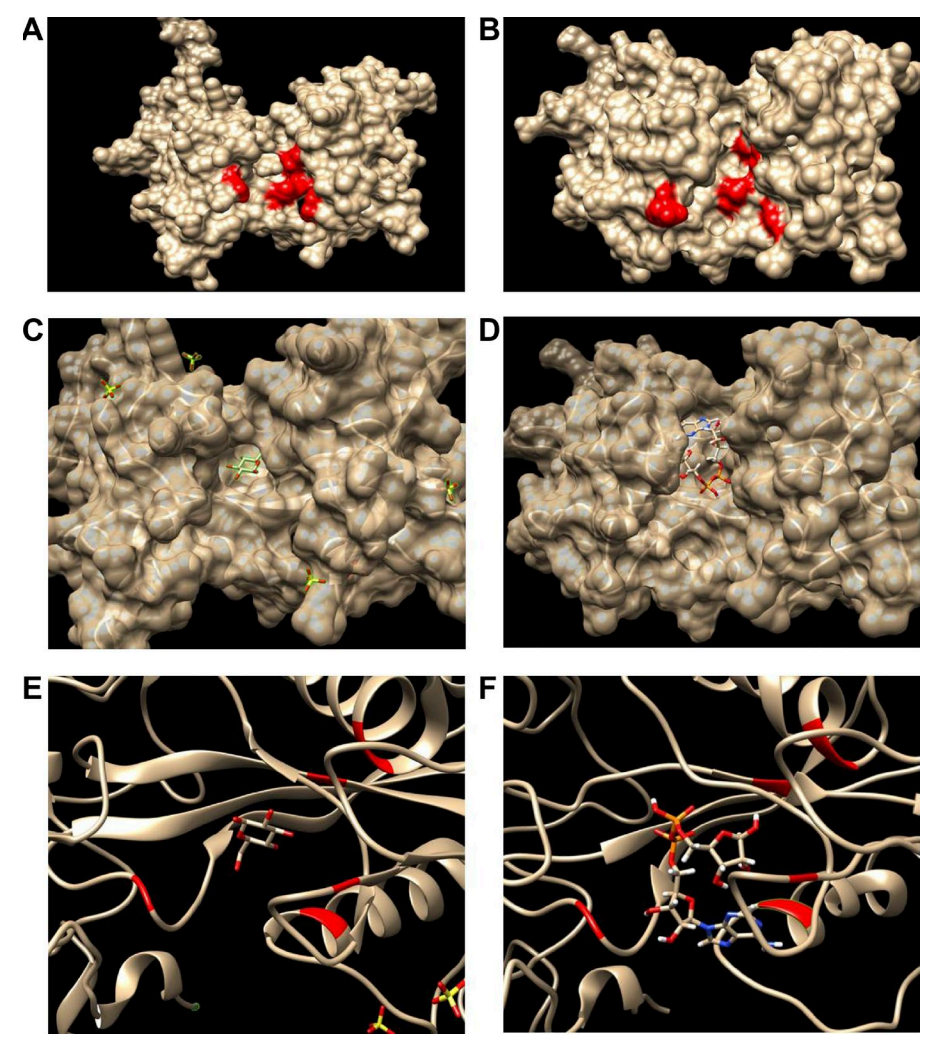


Figure 9. Molecular surface representation for the structure of the NUDT9 and NUDT9-H domains. (A) The side view of molecular surface representation for the NUDT9 structure. The previously proposed critical residues (W110, N168, M216, R273, M280, and D305) are highlighted in red. (B) The side view of molecular surface representation for the structure of NUDT9-H domain. The same critical residues shown in A are labeled in red. (C) Molecular surface representation for the structure of NUDT9 domain binding with R5P in the previously reported model. (D) Molecular surface representation for the structure of NUDT9-H domain binding with ADPR in our structure model. (E) D172, R204, E234, R273, and H324 residues labeled in red interact with R5P in the crystal structure of the NUDT9 protein. (F) Y1349, L1379, E1409, R1433, and H1488 residues that were reported to interact with R5P are labeled in in our NUDT9-H structure to interact with ADPR.

Moreau et al. (2013) synthesized several ADPR analogues and examined their effects on the function of TRPM2. They found that a compound, as modified with a phenyl group at C8 of the adenine and simultaneously modified with a 2'-deoxy motif at the adenosine ribose (8-phenyl-2-deoxy-ADPR), became a highly potent and specific antagonist with high affinity for the NUDT9-H domain (half-maximal inhibitory concentration of 3 µM). Consistently, our model has a cavity close to the purine ring of ADPR in the binding pocket that can accommodate a phenyl group (Fig. 7 A). Because only the C8-position-modified ADPR analogues exhibit highly antagonistic activities, the adenosine base of ADPR may very well be a critical factor in ADPR binding and gating of the TRPM2 channel. Finally, most of the residues identified in the present study have not been studied previously. The only exception is E1409, which was tested in two studies using an E-to-K mutation (Perraud et al., 2005; Tóth et al., 2014). The E1409K mutation was found to have little impact on ADPR binding to the NUDT9-H domain. Our simulations predicted no electrostatic interaction between the terminal ribose of ADPR and the hydroxyl oxygen atom of E1409. This prediction was further validated by our results from the E1409Q and E1409A mutants. Although we did not test the E1409K mutant, the reported results supported our model: by reversing the charge carried by the side chain, the E1409K mutation retained the polar solvation interaction but reversed the electrostatic interaction, further indicating that the electronic properties of E1409 do not affect ADPR binding to the NUDT9-H domain. All of these results further confirm the power and effectiveness of the methodological strategy of combining computation with experimental assays.

In summary, we revealed in this study the structural basis for ADPR binding to the NUDT9-H domain in the TRPM2 channel. Accumulating evidence has indicated TRPM2 is a potential therapeutic target for many diseases, and our findings will not only significantly advance the understanding of the molecular mechanisms of TRPM2 channel activation by ADPR, but will also provide the structural basis for future drug design efforts targeting the TRPM2 channel.

#### **ACKNOWLEDGMENTS**

The authors thank Prof. Jie Zheng, Dr. Fan Yang, and Dr. John Hugh Snyder for critical comments and reading the manuscript.

This work was supported by grants from the National Basic Research Program of China (2013CB910204 to W. Yang and 2014CB910300 to J. Luo) and the Natural Science Foundation of China (21402171 to P. Yu).

The authors declare no competing financial interests. Sharona E. Gordon served as editor.

Submitted: 29 July 2016 Revised: 12 October 2016 Accepted: 30 November 2016

#### REFERENCES

- Alim, I., L. Teves, R. Li, Y. Mori, and M. Tymianski. 2013. Modulation of NMDAR subunit expression by TRPM2 channels regulates neuronal vulnerability to ischemic cell death. *J. Neurosci.* 33:17264–17277. http://dx.doi.org/10.1523/JNEUROSCI.1729-13.2013
- Ashby, J.A., I.V. McGonigle, K.L. Price, N. Cohen, F. Comitani, D.A. Dougherty, C. Molteni, and S.C. Lummis. 2012. GABA binding to an insect GABA receptor: A molecular dynamics and mutagenesis study. *Biophys. J.* 103:2071–2081. http://dx.doi.org/10.1016/j.bpj.2012.10.016
- Csanády, L., and B. Törocsik. 2009. Four Ca<sup>2+</sup> ions activate TRPM2 channels by binding in deep crevices near the pore but intracellularly of the gate. *J. Gen. Physiol.* 133:189–203. http://dx.doi.org/10.1085/jgp.200810109
- Di, A., X.P. Gao, F. Qian, T. Kawamura, J. Han, C. Hecquet, R.D. Ye, S.M. Vogel, and A.B. Malik. 2012. The redox-sensitive cation channel TRPM2 modulates phagocyte ROS production and inflammation. *Nat. Immunol.* 13:29–34. http://dx.doi.org/10.1038/ni.2171
- Du, J., J. Xie, and L. Yue. 2009. Intracellular calcium activates TRPM2 and its alternative spliced isoforms. *Proc. Natl. Acad. Sci. USA*. 106:7239–7244. http://dx.doi.org/10.1073/pnas.0811725106
- Friesner, R.A., J.L. Banks, R.B. Murphy, T.A. Halgren, J.J. Klicic, D.T. Mainz, M.P. Repasky, E.H. Knoll, M. Shelley, J.K. Perry, et al. 2004.
  Glide: A new approach for rapid, accurate docking and scoring.
  Method and assessment of docking accuracy. J. Med. Chem. 47:1739–1749. http://dx.doi.org/10.1021/jm0306430
- Gao, G., W. Wang, R.K. Tadagavadi, N.E. Briley, M.I. Love, B.A. Miller, and W.B. Reeves. 2014. TRPM2 mediates ischemic kidney injury and oxidant stress through RAC1. J. Clin. Invest. 124:4989–5001. http://dx.doi.org/10.1172/JCI76042
- Iordanov, I., C. Mihályi, B. Tóth, and L. Csanády. 2016. The proposed channel-enzyme transient receptor potential melastatin 2 does not possess ADP ribose hydrolase activity. *eLife*. 5:e17600. http:// dx.doi.org/10.7554/eLife.17600
- Jiang, L.H., W. Yang, J. Zou, and D.J. Beech. 2010. TRPM2 channel properties, functions and therapeutic potentials. *Expert Opin. Ther. Targets.* 14:973–988. http://dx.doi.org/10.1517/14728222 .2010.510135
- Laskowski, R.A., M.W. Macarthur, D.S. Moss, and J.M. Thornton. 1993. PROCHECK: A program to check the stereochemical quality of protein structures. J. Appl. Cryst. 26:283–291. http://dx .doi.org/10.1107/S0021889892009944
- Lu, W., W. Fang, J. Li, B. Zhang, Q. Yang, X. Yan, L. Peng, H. Ai, J.J. Wang, X. Liu, et al. 2015. Phosphorylation of tyrosine 1070 at the GluN2B subunit is regulated by synaptic activity and critical for surface expression of N-methyl-D-aspartate (NMDA) receptors. J. Biol. Chem. 290:22945–22954. http://dx.doi.org/10.1074/jbc..M115.663450

- Manna, P.T., T.S. Munsey, N. Abuarab, F. Li, A. Asipu, G. Howell, A. Sedo, W. Yang, J. Naylor, D.J. Beech, et al. 2015. TRPM2-mediated intracellular Zn<sup>2+</sup> release triggers pancreatic β-cell death. *Biochem. J.* 466:537–546. http://dx.doi.org/10.1042/BJ20140747
- Massova, I., and P.A. Kollman. 2000. Combined molecular mechanical and continuum solvent approach (MM-PBSA/GBSA) to predict ligand binding. *Perspect. Drug Discov. Des.* 18:113–135. http://dx.doi.org/10.1023/A:1008763014207
- Miller, B.A., N.E. Hoffman, S. Merali, X.Q. Zhang, J. Wang, S. Rajan, S. Shanmughapriya, E. Gao, C.A. Barrero, K. Mallilankaraman, et al. 2014. TRPM2 channels protect against cardiac ischemiareperfusion injury: Role of mitochondria. *J. Biol. Chem.* 289:7615– 7629. http://dx.doi.org/10.1074/jbc.M113.533851
- Moreau, C., T. Kirchberger, J.M. Swarbrick, S.J. Bartlett, R. Fliegert, T. Yorgan, A. Bauche, A. Harneit, A.H. Guse, and B.V. Potter. 2013. Structure-activity relationship of adenosine 5'-diphosphoribose at the transient receptor potential melastatin 2 (TRPM2) channel: Rational design of antagonists. *J. Med. Chem.* 56:10079–10102. http://dx.doi.org/10.1021/jm401497a
- Perraud, A.L., A. Fleig, C.A. Dunn, L.A. Bagley, P. Launay, C. Schmitz, A.J. Stokes, Q. Zhu, M.J. Bessman, R. Penner, et al. 2001. ADP-ribose gating of the calcium-permeable LTRPC2 channel revealed by Nudix motif homology. *Nature*. 411:595–599. http://dx.doi.org/10.1038/35079100
- Perraud, A.L., B. Shen, C.A. Dunn, K. Rippe, M.K. Smith, M.J. Bessman, B.L. Stoddard, and A.M. Scharenberg. 2003. NUDT9, a member of the Nudix hydrolase family, is an evolutionarily conserved mitochondrial ADP-ribose pyrophosphatase. *J. Biol. Chem.* 278:1794–1801. http://dx.doi.org/10.1074/jbc..M205601200
- Perraud, A.L., C.L. Takanishi, B. Shen, S. Kang, M.K. Smith, C. Schmitz, H.M. Knowles, D. Ferraris, W. Li, J. Zhang, et al. 2005. Accumulation of free ADP-ribose from mitochondria mediates oxidative stress-induced gating of TRPM2 cation channels. J. Biol. Chem. 280:6138–6148. http://dx.doi.org/10.1074/jbc..M411446200
- Qian, X., T. Numata, K. Zhang, C. Li, J. Hou, Y. Mori, and X. Fang. 2014. Transient receptor potential melastatin 2 protects mice against polymicrobial sepsis by enhancing bacterial clearance. *Anesthesiology*. 121:336–351. http://dx.doi.org/10.1097/ALN .00000000000000275
- Sano, Y., K. Inamura, A. Miyake, S. Mochizuki, H. Yokoi, H. Matsushime, and K. Furuichi. 2001. Immunocyte Ca<sup>2+</sup> influx system mediated by LTRPC2. *Science*. 293:1327–1330. http://dx.doi.org/10.1126/science.1062473
- Shen, B.W., A.L. Perraud, A. Scharenberg, and B.L. Stoddard. 2003. The crystal structure and mutational analysis of human NUDT9. *J. Mol. Biol.* 332:385–398. http://dx.doi.org/10.1016/S0022-2836(03)00954-9
- Song, K., H. Wang, G.B. Kamm, J. Pohle, F.C. Reis, P. Heppenstall, H. Wende, and J. Siemens. 2016. The TRPM2 channel is a hypothalamic heat sensor that limits fever and can drive hypothermia. *Science*. 353:1393–1398 (P). http://dx.doi.org/10 .1126/science.aaf7537
- Starkus, J., A. Beck, A. Fleig, and R. Penner. 2007. Regulation of TRPM2 by extra- and intracellular calcium. *J. Gen. Physiol.* 130:427–440. http://dx.doi.org/10.1085/jgp.200709836
- Tan, C.H., and P.A. McNaughton. 2016. The TRPM2 ion channel is required for sensitivity to warmth. *Nature*. 536:460–463. http:// dx.doi.org/10.1038/nature19074
- Tóth, B., and L. Csanády. 2012. Pore collapse underlies irreversible inactivation of TRPM2 cation channel currents. *Proc. Natl. Acad. Sci. USA*. 109:13440–13445. http://dx.doi.org/10.1073/pnas.1204702109

- Tóth, B., I. Iordanov, and L. Csanády. 2014. Putative chanzyme activity of TRPM2 cation channel is unrelated to pore gating. *Proc. Natl. Acad. Sci. USA*. 111:16949–16954. http://dx.doi.org/10.1073/pnas.1412449111
- Tóth, B., I. Iordanov, and L. Csanády. 2015. Ruling out pyridine dinucleotides as true TRPM2 channel activators reveals novel direct agonist ADP-ribose-2'-phosphate. J. Gen. Physiol. 145:419– 430. http://dx.doi.org/10.1085/jgp.201511377
- Uchida, K., K. Dezaki, B. Damdindorj, H. Inada, T. Shiuchi, Y. Mori, T. Yada, Y. Minokoshi, and M. Tominaga. 2011. Lack of TRPM2 impaired insulin secretion and glucose metabolisms in mice. *Diabetes*. 60:119–126. http://dx.doi.org/10.2337/db10-0276
- Weiss, J.N. 1997. The Hill equation revisited: Uses and misuses. *FAS EB J.* 11:835–841.
- Yamamoto, S., S. Shimizu, S. Kiyonaka, N. Takahashi, T. Wajima, Y. Hara, T. Negoro, T. Hiroi, Y. Kiuchi, T. Okada, et al. 2008. TRPM2-mediated Ca<sup>2+</sup>influx induces chemokine production in monocytes that aggravates inflammatory neutrophil infiltration. *Nat. Med.* 14:738–747. http://dx.doi.org/10.1038/nm1758
- Yang, F., X. Xiao, W. Cheng, W. Yang, P. Yu, Z. Song, V. Yarov-Yarovoy, and J. Zheng. 2015. Structural mechanism underlying capsaicin binding and activation of the TRPV1 ion channel. *Nat. Chem. Biol.* 11:518–524. http://dx.doi.org/10.1038/nchembio.1835
- Yang, W., J. Zou, R. Xia, M.L. Vaal, V.A. Seymour, J. Luo, D.J. Beech, and L.H. Jiang. 2010. State-dependent inhibition of TRPM2

- channel by acidic pH. J. Biol. Chem. 285:30411–30418. http://dx.doi.org/10.1074/jbc.M110.139774
- Yang, W., P.T. Manna, J. Zou, J. Luo, D.J. Beech, A. Sivaprasadarao, and L.H. Jiang. 2011. Zinc inactivates melastatin transient receptor potential 2 channels via the outer pore. *J. Biol. Chem.* 286:23789–23798. http://dx.doi.org/10.1074/jbc.M111.247478
- Ye, M., W. Yang, J.F. Ainscough, X.P. Hu, X. Li, A. Sedo, X.H. Zhang, X. Zhang, Z. Chen, X.M. Li, et al. 2014. TRPM2 channel deficiency prevents delayed cytosolic Zn<sup>2+</sup> accumulation and CA1 pyramidal neuronal death after transient global ischemia. *Cell Death Dis.* 5:e1541. http://dx.doi.org/10.1038/cddis.2014.494
- Yu, W., L.H. Jiang, Y. Zheng, X. Hu, J. Luo, and W. Yang. 2014. Inactivation of TRPM2 channels by extracellular divalent copper. PLoS One. 9:e112071. http://dx.doi.org/10.1371/journal.pone. 0112071
- Zhang, X.M., X.Y. Yan, B. Zhang, Q. Yang, M. Ye, W. Cao, W.B. Qiang, L.J. Zhu, Y.L. Du, X.X. Xu, et al. 2015. Activity-induced synaptic delivery of the GluN2A-containing NMDA receptor is dependent on endoplasmic reticulum chaperone Bip and involved in fear memory. *Cell Res.* 25:818–836. http://dx.doi.org/10.1038/cr.2015.75
- Zhou, L., and S.A. Siegelbaum. 2007. Gating of HCN channels by cyclic nucleotides: Residue contacts that underlie ligand binding, selectivity, and efficacy. *Structure*. 15:655–670. http://dx.doi.org/10.1016/j.str.2007.04.012